Bioactive Materials 7 (2022) 377–388

Contents lists available at ScienceDirect

Bioactive Materials

journal homepage: www.sciencedirect.com/journal/bioactive-materials

Tumor acid microenvironment-activated self-targeting & splitting gold nanoassembly for tumor chemo-radiotherapy

Xiaomin Li [a], Licheng Yu [a], Chuangnian Zhang [b,**], Xiaoyan Niu [a], Mengjie Sun [a], Zichao Yan [a], Wei Wang [a], Zhi Yuan [a,c,*]

[a] Key Laboratory of Functional Polymer Materials of Ministry of Education, College of Chemistry, Nankai University, Tianjin, 300071, China
[b] Tianjin Key Laboratory of Biomaterial Research, Biomedical Barriers Research Center, Institute of Biomedical Engineering, Chinese Academy of Medical Science & Peking Union Medical College, Tianjin, 300192, China
[c] Collaborative Innovation Center of Chemical Science and Engineering, Nankai University, Tianjin, 300071, China

ARTICLE INFO

Keywords:
Gold nanoassembly
Disassemble
Penetration
Self-target
Chemo-radiotherapy

ABSTRACT

Low accumulation and penetration of nanomedicines in tumor severely reduce therapeutic efficacy. Herein, a pH-responsive gold nanoassembly is designed to overcome these problems. Polyethylene glycol linked raltitrexed (RTX, target ligand and chemotherapy drug) and two tertiary amine molecules (1-(2-aminoethyl) pyrrolidine and *N, N*-dibutylethylenediamine) are modified on the surface of the 6-nm gold nanoparticles by lipoic acid to form gold nanoassembly defined as Au-NNP(RTX). The Au-NNP (RTX) nanoassembly could remain at about 160 nm at the blood circulation (pH 7.4), while split into 6-nm gold nanoparticles due to tertiary amine protonation at tumor extracellular pH (pH 6.8). This pH-responsive disassembly behavior endows Au-NNP(RTX) better tumor tissue permeability through the better diffusion brought by the size reduction. Meanwhile, after disassembly, more RTXs on the surface of gold nanoparticles are exposed from the shielded state of assembly along with 2.25-fold augment of cellular uptake capability. Most importantly, the results show that Au-NNP(RTX) possesses of high tumor accumulation and effective tumor penetration, thereby enhancing the tumor chemo-radiotherapy efficiency.

1. Introduction

Although tumor therapy has achieved great progress in recent decades, therapeutic effect still needs to be improved [1,2]. For numerous nanomedicines, therapeutic efficiency heavily depends on the role of nanomedicines in the body, thus many efforts have been devoted to explore it. Researches show that nanomedicines injected into the body usually would go through five processes: 1) blood circulation; 2) tumor accumulation; 3) tumor penetration; 4) cellular internalization; and 5) drug release (exerting therapeutic effect in the tumor cells [3]). It turns out that curative effect is restricted by each of the above steps [4]. Generally, to achieve better curative effect, nanomedicines are required to have the following abilities: 1) blood circulation stability to avoid being recognized and eliminated by the immune system; 2) sufficient tumor accumulation, deep tumor penetration to guarantee therapeutic dose in the tumor; and 3) high tumor cell targeting to ensure enough cellular internalization of nanomedicines [4]. With regard to this, some demands for the size and surface properties of nanomedicines are put forward.

Studies have found that the size of nanomedicines should keep at 10–500 nm for better blood circulation, since the nanomedicines (>500 nm and <10 nm) are easily and quickly cleared by the lungs and kidneys, respectively [5]. While the smaller nanomedicines are more conducive to penetration in the tumor, such as 3–7 nm ultrasmall platinum nanoparticles [6–13]. Moreover, to avoid being recognized and eliminated by the immune system, the surface electrical properties of nanomedicines are best to maintain neutral or negative [10], and the hydrophobic targeting ligands are not exposed on the surface as much as possible. However, nanomedicines with positive surface are easier to bind to negatively charged cell membranes for better cellular internalization [14–16]. Nanomedicines with targeting ligands exposed on the surface are also easier to enter the tumor cells, thus improving the tumor

Peer review under responsibility of KeAi Communications Co., Ltd.
* Corresponding author. Collaborative Innovation Center of Chemical Science and Engineering, Nankai University, Tianjin, 300071, China.
** Corresponding author.
E-mail addresses: cnzhang@mail.nankai.edu.cn (C. Zhang), zhiy@nankai.edu.cn (Z. Yuan).

https://doi.org/10.1016/j.bioactmat.2021.05.050
Received 23 February 2021; Received in revised form 29 May 2021; Accepted 29 May 2021
Available online 10 June 2021

accumulation and cellular internalization [17–22]. Contradictory demands for size and surface of nanomedicines at blood circulation and tumor site have brought new difficulties to the design of nanomedicines.

Recently, the intelligent control of size and surface properties of nanomedicines at different stages has been proposed to solve the above contradictions [23–27]. Zhou et al. developed a near-infrared (NIR) light triggered disintegrable liposomal nanoplatform (PAM/Pt@IcLipo, ~162 nm) [24]. When irradiated by NIR light at tumor site, the releasing small-sized PAM/Pt nanoparticles (~8.6 nm) from the liposomes were capable of penetrating into the deep tumor tissue. Qu et al. designed a tumor-activatable ultrasmall nanozyme generation, with the aid of mildly tumor acid microenvironment, the produced gluconic acid from intratumoral glucose can gradually induce the dissociation of ZIF-8 to release ultrasmall peroxidase nanozyme with significant intratumoral penetration [25]. Sun et al. developed a pH-responsive charge switchable PEGylated epsilon-poly-L-lysine polymeric nanoparticle to facilitate cell internalization and deep tumor penetration, thus improving breast cancer treatment [26]. These intelligent (pH, enzyme, NIR light)-responsive size decrease and charge reverse of nanomedicines have been proved to prolong the blood circulation and improve the tumor accumulation and penetration. However, how to design nanomedicines with reasonable size and surface to adapt the tumor environment is not easy and implementing these in one simple way is still an obstacle.

Previously, we have constructed a pH-sensitive self-assembly/disassembly system of gold nanoparticles (Au NPs, ~15 nm) to shield liver targeting ligand (glycyrrhetinic acid) at the blood circulation and deshield it at tumor site, demonstrating that reversible shielding of ligand can effectively improve tumor accumulation and cellular internalization [17,28]. In this work, we have constructed a system to achieve both high-efficiency tumor accumulation and penetration of nanomedicines, as shown in Scheme 1. Polyethylene glycol (PEG) linked raltitrexed (RTX, targeting and chemotherapeutic effects) and two small tertiary amine molecules (*N*, *N*-dibutylethylenediamine defined as NR_1 and 1-(2-aminoethyl) pyrrolidine defined as NR_2) were modified to the surface of Au NPs (~6 nm) by lipoic acid (LA) to form gold nanoassembly defined as Au-NNP(RTX). At the blood circulation, Au-NNP (RTX) could keep assembled and most RTXs are hidden inside the nanoassembly. While at the mildly tumor acid microenvironment (pH = 6.8), the nanoassembly could disassmble and split into 6-nm Au NPs which is expected to achieve better penetration via elevated diffusion (*i enhanced penetration*). After disassembled, the RTXs hidden inside are also exposed simultaneously to enhance tumor targeting (*ii enhanced targeting*) and chemotherapy. Moreover, radiotherapy (RT) sensitization of gold element and chemotherapy effect of RTX simultaneously act on tumor cells, which is expected to achieve better therapeutic effects (*iii chemo-radiotherapy*).

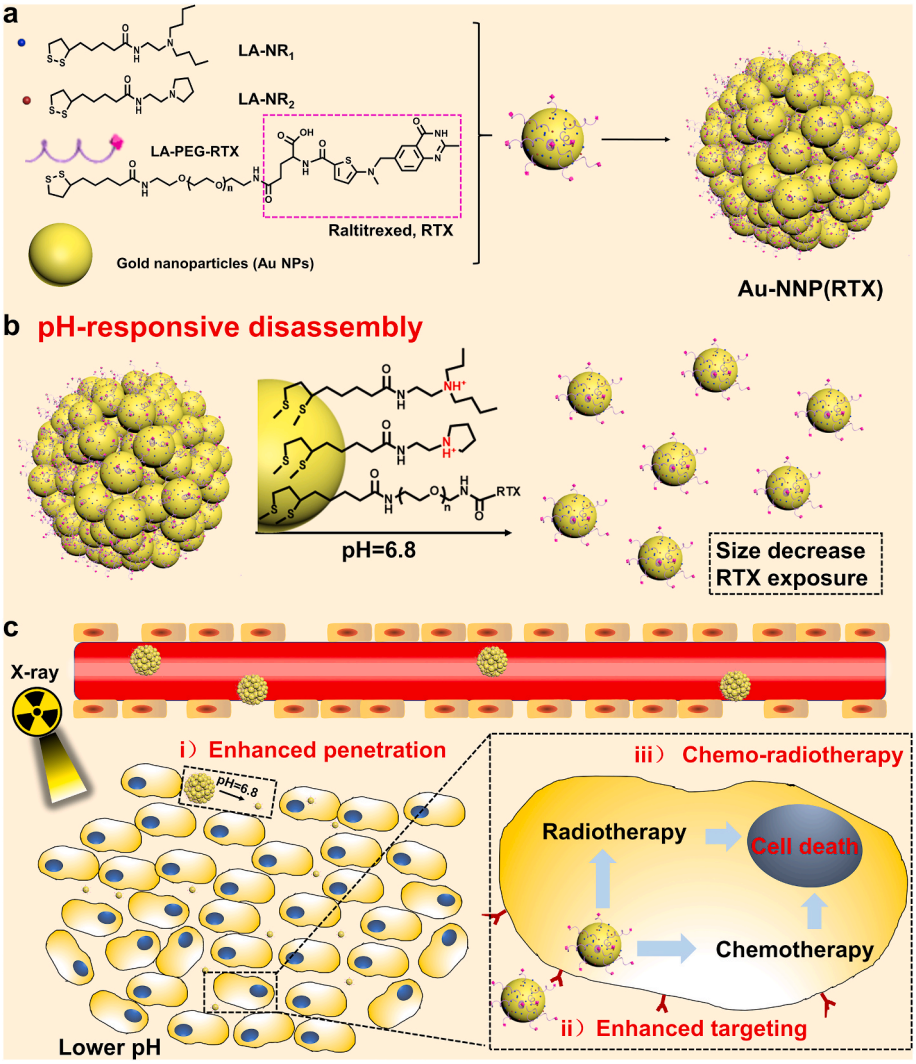

Scheme 1. Schematic illustration of **a** preparation of Au-NNP(RTX) nanoassembly; **b** pH-responsive disassembly process; **c** *in vivo* possible process.

2. Experimental section

2.1. Materials, cells and animal

Tetrachloroauric acid trihydrate was purchased from Shanghai Dibo Biological Technology Co., Ltd. Sodium citrate dehydrate was purchased from Tianjin Alpha Biotechnology Co., Ltd. Sodium borohydride was purchased from Beijing Innochem Technology Co., Ltd. RTX, *N*-Hydroxy succinimide (NHS) and *N*-(3-(Dimethylamino)propyl)-*N*′-ethyl-carbodiimide hydrochloride (EDC), FITC were purchased from Shanghai Aladdin Bio-Chem Technology Co., Ltd. Amino polyethylene glycol lipoic acid (LA-PEG-NH_2, Mw_{PEG} = 2000) is purchased from Shanghai Tuoyang Biological Technology Co., Ltd. 4-Dimethylaminopyridine (DMAP) was purchased from Shanghai New Platinum Chemical Technology Co., Ltd. Folic acid (FA) was purchased from Tianjin Heowns Co., Ltd.

4′, 6-diamidino-2-phenylindole (DAPI), 3-(4, 5-dimethyl-2-thiazolyl)-2,5-diphenyl-2-H-tetrazolium bromide (MTT), acridine orange/ethidium bromide (AO/EB) staining kit, annexin V-FITC/PI apoptosis detection Kit and RNase-propidium iodide were purchased from Tianjin Solomon Biotech, Inc. Anti-CD31/FITC mouse ELISA Kit was purchased from Beijing Boaosen Biotechnology Co., Ltd. Dimethyl sulfoxide (DMSO), absolute ethanol, hydrochloric acid (HCl), nitric acid (HNO_3) and sodium hydroxide (NaOH) were purchased from Tianjin Chemical Reagent Supply and Marketing Company. The D.I. water used in this work was provided by Millipore Elix System (Millipore, USA, Bedford).

Murine colon adenocarcinoma CT26 cells provided by Institute of Biomedical Engineering, Chinese Academy of Medical Science & Peking Union Medical College (Tianjin, China) were cultured in RPMI 1640 medium containing 10% fetal bovine serum (FBS) in a standard cell culture environment (humidified, 37 °C, 5% CO_2). HepG2 cells provided by the same company were cultured in DMEM medium containing 10% FBS in the same environment (humidified, 37 °C, 5% CO_2). BALB/c mice (female, 6–8 weeks) were provided by Beijing Vital River Laboratory Animal Technology Co., Ltd. All animal procedures were reviewed and ethically approved by Center of Tianjin Animal Experiment Ethics Committee and Authority for animal protection (Approval No.: SYXK (Jin) 2011–0008).

2.2. Synthesis of Au NPs

Tetrachloroauric acid aqueous solution (0.6 mL, 10 mg/mL) and sodium citrate aqueous solution (0.6 mL, 10 mg/mL) were added in 60 mL D.I. water. After fully mixing, 11.4 mg sodium borohydride dissolved in 3 mL cold D.I. water was quickly added into the mixed solution and reacted for 1 h. Then the 6-nm Au NPs were prepared and measured by transmission electron microscope (TEM, HT7700, Japan, Hitachi), dynamic light scattering (DLS, ZS90, Britain, Malvern) and UV–Vis spectrum (ZF-IA, China, Heqin).

2.3. Synthesis of LA-PEG-RTX

RTX (91.7 mg), EDC (76.7 mg) and NHS (46.0 mg) were added into 5 mL DMSO and reacted under stirring at 40 °C for 3 h to activate the carboxyl group on RTX. Then add LA-PEG-NH_2 (330 mg) in the mixture and react at 40 °C for 12 h. It was then precipitated with ice ether, dialyzed in aqueous solution for 72 h and freeze-dried to obtain a light-yellow solid (LA-PEG-RTX) with a yield of 57.2%. FT-IR and MALDI-TOF MS spectra of LA-PEG-RTX were measured.

2.4. Modification and self-assembly of Au NPs

LA-PEG-RTX (1.0 μmol), LA-NR_1 (22.5 μmol) and LA-NR_2 (7.5 μmol) were dissolved in 1 mL D.I. water, and add HCl to make its pH value 4.0. Then add 10 mL Au NPs and react for 2 h under stirring. After that, several drops of NaOH solution (1 mM) were added into the solution under slow stirring until its color turned purple-red. The obtained Au-NNP(RTX) nanoassembly was centrifuged for purification. The control group-Au-NP(RTX) used in the follow-up experiment was prepared by similar method with small modification (no LA-NR_2). FT-IR spectra of nanoassembly was measured.

2.5. RTX modification

RTX solutions at different concentrations (2.5, 5, 10, 20 and 40 μg/mL) were prepared and measured by UV–Vis spectrum. The standard curve line of RTX was calculated. Then we measured the UV–Vis spectrum of reaction supernatant after dialysis, lyophilization and re-dissolving to calculate the RTX content in the supernatant. And the modification amount of RTX can be calculated by subtracting the RTX content in the supernatant from the total feed. The Au NPs in the reaction solution can be measured by Nanoparticle tracking analyzer (NS300, Britain, Malvern).

2.6. pH-sensitive behavior study

Au-NNP(RTX) (100 μL, 50 μg/mL) was added into 900 μL PBS buffer with different pHs (7.4, 7.2, 7.0, 6.8, 6.6, 6.4, 6.2 and 6.0). 1 h later, the hydrodynamic diameters of these mixtures were measured by DLS. Au-NNP(RTX) (100 μL, 50 μg/mL) were added into 900 μL PBS buffer and RPMI 1640 (10% FBS), respectively. Hydrodynamic diameters of these mixtures were measured by DLS at 0, 1.5, 3, 6, 12, 24 and 48 h. Then the Au-NNP(RTX) and Au-NP(RTX) (100 μL, 50 μg/mL) were added into 900 μL PBS buffer with different pHs (7.4 and 6.8). Moreover, these mixtures were measured by TEM and DLS.

2.7. In vitro hemolysis assay

The *in vitro* hemolysis assay of Au-NNP(RTX) nanoassembly was measured to evaluate the blood compatibility. Ethylenediaminetetraacetic acid (EDTA)-stabilized mice blood samples were freshly collected from BALB/c mice to get RBCs. Firstly, 1 mL of blood sample was added to 2 mL of PBS, and then the serum was removed from erythrocyte cells by centrifugation at 3000 rpm for 10 min, the erythrocyte cells were further washed three times and resuspended in 5 mL PBS. The Au-NNP (RTX) nanoassemblies at different concentrations of 6.25, 12.5, 25, 50, 100 and 200 μg/mL were incubated with erythrocyte cells suspension at room temperature for 2 h. D.I. water was used as the positive control, and PBS was the negative control. At last, the mixtures were centrifuged at 3000 rpm for 10 min, and the absorbance values of the supernatants were determined by Microplate reader at a test wavelength of 570 nm. The percentage of hemolysis was calculated by: hemolysis % = (sample absorbance-negative control absorbance)/(positive control absorbance-negative control absorbance) × 100.

2.8. Flow cytometry analysis

To visually observe and analyze cellular uptake, the nanoassemblies labeled with FITC (modified on PEG using the same synthesis method as LA-PEG-RTX). CT26 cells at a density of 1×10^5 cells/well were seeded in two 6-well plates and cultured for 24 h. They were divided into three groups, and one is deal with free FA (100 μM) 1 h in advance. FITC labeled Au-NNP(RTX) (10 μg/mL, newly prepared medium at pH 6.8) was added into FA-pretreated group and another, and then incubated for another 4 h. After being washed by PBS and cooled PBS for several times, the cells were collected by centrifugation and resuspended in 0.5 mL pre-cooled PBS for fully dispersion. Moreover, the fluorescence signal of FITC was analyzed by flow cytometry (FACS Calibur, USA, BD). The same experiment is conducted to HepG2 cells.

2.9. Cellular uptake

CT26 cells at a density of 5×10^4 cells/well were seeded in the confocal dishes and cultured for 24 h. FITC-labeled Au-NNP(RTX) (10 μg/mL in newly prepared medium at pH 7.4 and 6.8) were added into the dishes and incubated for another 4 h. After being washed by PBS for three times, the cells were stained with DAPI and Lyso-Tracker Red, respectively, and then observed by laser scanning confocal microscope (CLSM, A1+, Japan, Nikon).

Then, CT26 cells were cultured and divided into two groups, and one is deal with free FA in advance. FITC-labeled Au-NP(RTX) and Au-NNP (RTX) (10 μg/mL in newly prepared medium at pH 7.4 and 6.8) were added into the dishes and incubated for another 4 h, After being washed by PBS for three times, the CT26 cells were observed by CLSM. Besides, the same experiment was finished with small modification (irradiated by X-ray at a dose of 2 Gy 1 h in advance).

2.10. In vitro ICP experiment

CT26 cells at a density of 2×10^4 cells/well were seeded in 5 48-well plates and cultured for 24 h. The plates were irradiated with different X-ray doses of 0, 2, 4, 6 and 8 Gy, respectively and cultured for 1 h. Then Au-NNP(RTX) and Au-NP(RTX) nanoassemblies (10 μg/mL in newly prepared medium at different pHs: pH 7.4 and 6.8 for 0 and 2-Gy groups, pH 6.8 for 4, 6 and 8-Gy groups) were added into the dishes respectively and incubated for another 4 h. After that, the cells were washed by PBS for three times. Subsequently, add 100 μL aqua regia to dissolve the cells, and test with Inductively Coupled Plasma-Atomic Emission Spectrometry (ICP-AES, Optima 8300, Germany, PerkinElmer) after centrifugation and dilution.

2.11. Cell cycle

CT26 cells at a density of 1×10^5 cells/well were seeded in two 6-well plates and cultured for 24 h. Au-NP(RTX) and Au-NNP(RTX) nanoassemblies (50 μg/mL, newly prepared medium at pH 6.8) were added into the wells of both plates and incubated for another 4 h, each plate sets a control group. After being washed by PBS for three times, the CT26 cells in one plate were irradiated by X-ray at a dose of 2 Gy, and the other is not. The cells in both plates were incubated for another 12 h and collected by centrifugation. Ather being washed by cooled PBS several times, the cells were resuspended in 0.5 mL pre-cooled PBS for fully dispersion and added with 2 mL absolute ethanol for fixing the cells. After being placed at 4 °C overnight, the cells were centrifuged to remove the ethanol aqueous solution, stained by RNase-propidium iodide solution for 30 min at 37 °C. The PI fluorescence signal was analyzed by flow cytometry.

2.12. Cytotoxicity

CT26 cells at a density of 8×10^3 cells/well were seeded in two 96-well plates and cultured for 24 h. RTX, Au-NP(RTX) and Au-NNP(RTX) at the concentrations of 0, 25, 50, 100 and 200 μg/mL (newly prepared with medium at pH 6.8) were added into the wells and incubated for 24 h. After being washed by PBS for three times, CT26 cells in one plate were irradiated by X-ray at a dose of 2 Gy, and the cells in both two plates were incubated for another 18 h. In addition, the following process is strictly in accordance with standard operation manual of MTT assay. The absorbance in every well was measured by Microplate reader.

2.13. AO/EB staining

CT26 cells at a density of 5×10^4 cells/well were seeded in confocal dish and divided into two groups. 24 h later, the two groups were added with RTX, Au-NP(RTX) and Au-NNP(RTX) (50 μg/mL, newly prepared with medium at pH 6.8) respectively and incubated for another 4 h. After being washed by PBS for three times, the CT26 cells in one group were irradiated by X-ray at a dose of 2Gy, and the other one is not. The CT26 cells in both groups were incubated for another 18 h and stained by acridine orange (AO, 0.1 mg/mL) and ethidium (EB, 0.1 mg/mL). Then the live and dead cells were observed by CLSM.

2.14. Cell apoptosis

CT26 cells at a density of 1×10^5 cells/well were seeded in two 6-well plates and cultured for 24 h. RTX, Au-NP(RTX) and Au-NNP (RTX) (50 μg/mL, newly prepared medium at pH 6.8) were added into the wells of both plates and incubated for another 4 h, each plate sets a control group. After being washed by PBS for three times, the CT26 cells in one plate were irradiated by X-ray at a dose of 2 Gy, and the other is not. The cells in both plates were incubated for another 18 h and collected by centrifugation. Then the cells were washed twice with pre-cooled PBS, resuspended in 0.1 mL 1 × Binding Buffer, stained by 5 μL Annexin V-FITC for 10 min and 5 μL PI for 5 min. Flow cytometry was used to analyze apoptosis of these cells.

2.15. Penetration into CT26 multicellular spheroids

CT26 cells at a density of 3×10^5 cells/well were seeded in an ultra-low adhesion 6-well plate, and cultured for 48 h. When the size of CT26 multicellular spheroids (MCSs) reached 200 μm, Cy5-labeled Au-NP (RTX) and Au-NNP(RTX) (100 μg/mL) (same as FITC-labeled ones) were added and incubated for 4 h. After careful washing with PBS, the penetrations of Au-NP(RTX) and Au-NNP(RTX) in MCSs were observed by CLSM.

2.16. In vivo penetration

The tumor xenograft model is established by subcutaneously injecting 1×10^6 CT26 cells into the right oxter of BALB/c mice. When the mean tumor volume reached about 50 mm^3, the mice bearing CT26 tumor were randomly divided into three groups. Cy5-labeled Au-P (RTX), Au-NP(RTX), Au-NNP(RTX) (Au: 10 mg/kg) were injected into the mice via tail vein. The mice were sacrificed and the tumors were taken out after 12 h. The tumors were dehydrated with 30% sugar solution for 48 h, fixed with 4% formaldehyde for 48 h, and cut into 8 μm thick sections. Then the sections were stained by DAPI and Anti-CD31/FITC according to the standard procedure and observed by CLSM.

2.17. In vivo fluorescence imaging

When the mean tumor volume reached about 50 mm^3, the mice bearing CT26 tumor were randomly divided into three groups. Cy5-labeled Au-P(RTX), Au-NP(RTX), Au-NNP(RTX) (Au: 10 mg/kg) were injected into the mice via tail vein. *In vivo* fluorescence imaging of the mice was detected at 6, 12 and 24 h by *in vivo* fluorescence imaging system (IVIS Lumina II, USA, Caliper Life Sciences). The detailed camera operation: First, collect the bright field images. To avoid the interference of signal from other organs, the mice were sheltered by black cardboards except for the tumor site before fluorescence imaging. Finally, the fluorescence signal from the tumor acquired by small animal *in vivo* imaging system overlapped with the bright field image of mice. Moreover, we also measured the *ex vivo* fluorescence imaging of heart, liver, spleen, lung, kidney and tumor excised from sacrificed mice 24 h after injection of Cy5-labeled Au-P(RTX), Au-NP(RTX) and Au-NNP(RTX).

2.18. Biodistribution experiment

When the mean tumor volume reached about 50 mm^3, the mice bearing CT26 tumor were randomly divided into three groups. Au-P (RTX), Au-NP(RTX), Au-NNP(RTX) (Au: 10 mg/kg) were injected into the mice via tail vein. 12 h later, all the mice were sacrificed, and

approximately 500 μL blood samples were collected from each mouse, and heart, liver, spleen, lung, kidney and tumor of each mouse were taken out. Then weigh and dissolve them in aqua regia. The Au element in these tissues, tumor and blood were detected by ICP-AES.

2.19. In vivo antitumor study

When the mean tumor volume reached about 50 mm^3, the mice bearing CT26 tumor were randomly divided into eight groups (PBS, PBS+RT, RTX, Au-NNP(RTX), RTX+RT, Au-P(RTX)+RT, Au-NP(RTX)+RT, Au-NNP(RTX)+RT, n = 6). The nanoparticles (Au: 10 mg/kg) were injected into the mice via tail vein. Then the mice were irradiated by X-ray at the dose of 4 Gy after 2 h and 12 h accumulation in tumor, respectively. The body weight and the tumor size were measured every two days. At 14 day, the mice were euthanized, and approximately 500 μL blood samples were collected from each mouse (PBS, Au-NNP(RTX) and Au-NNP(RTX)+RT groups), followed by blood biochemistry analysis. The items included white blood cell (WBC), lymphocyte (LYM), red blood cell (RBC), hemoglobin (HGB), hematocrit (HCT), mean corpuscular volume (MCV), mean corpuscular hemoglobin (MCH), Mean corpuscular hemoglobin concentration (MCHC), red cell distribution width (RDW), platelet (PLT), mean platelet volume (MPV). The tumors of all sacrificed mice were pictured and weighed. The major organs (heart, liver, spleen, lung and spleen) of these eight groups were taken out and washed with PBS several times, and finally fixed in 4% paraformaldehyde. According to standard protocols of hematoxylin & eosin (H&E) staining, the sections were pictured by optical microscope (IX53, Japan, Olympus).

2.20. Statistical analysis

The results are representative of replicate experiments and are presented as the mean value with standard deviation (mean ± SD). Student's t-test was used to compare the differences in the results. *$p < 0.05$ was considered statistically significant. **(#)$p < 0.01$ were considered extremely significant.

3. Results and discussion

3.1. Characterization and pH-responsive disassembly of Au-NNP(RTX)

To obtain pH-responsive Au-NNP(RTX) nanoassembly, naked Au NPs were firstly synthesized and the TEM, DLS and UV–Vis spectrum results in Fig. S1 indicate the successful preparation of ~ 6-nm spherical Au NPs. This size of Au NPs is conductive to tumor penetration, taking feasibility of surface modification into account. LA-PEG-RTX was then synthesized via amidation reaction and the synthetic route is shown in Fig. S2. The FT-IR spectra in Fig. S3 shows that strong transmission peaks at 1737 cm^{-1} and 1713 cm^{-1} indicate the presence of carboxylic acid, and the peak at 1615 cm^{-1} illustrates the presence of aromatic ring, both of which prove that RTX has bonded to LA-PEG-NH_2. Also, the MALDI-TOF MS spectra in Fig. S4 shows that the molecular weight distribution conforms to the theoretical values. The above results all indicate the successful synthesis of LA-PEG-RTX. The synthesis of LA-NR_1 and LA-NR_2 has been reported in our previous work [29].

Then Au-NNP(RTX) nanoassembly is prepared according to the pH-sensitive assembly/disassembly strategy proposed by our research group [29,30]. LA-PEG-RTX, LA-NR_1 and LA-NR_2 were co-modified on the surface of 6-nm Au NPs by stirring at room temperature. The FT-IR spectra in Fig. S6 shows that the presence of strong transmission peaks at 1672 cm^{-1} (amide I bond) and 1523 cm^{-1} (amide II bond) has confirmed that many substances containing amide bonds on the surface of Au NPs. In addition, the peak at 1103 cm^{-1} (carbon-oxygen bond) illustrates that the LA-PEG-RTX is successfully modified on the surface of the Au NPs. And the peaks at 1376 and 2957 cm^{-1} indicate the presence of LA-NR_1 on the surface of Au NPs. Besides, we calculated the modification amount of RTX in 11 mL reaction solution by subtracting the RTX content in the supernatant from the total feed. In Fig. S5a, the standard curve line of RTX is $y = 0.05376x+0.00537$, y is absorbance values, x is concentration of RTX (μg/mL) and the absorbance value of the RTX in the supernatant (in 11 mL reaction solution) is 1.911 (Fig. S5b). Thus, the amount of RTX modified with 10 mL Au NPs is 0.068 mg and the number of RTX is calculated to be 9×10^{16}. Then we employed Nanoparticle tracking analyzer to detect the numbers of Au NPs and there are about 1.5×10^{15} Au NPs in the same solution. Thus it can be seen that per Au NP approximately contains 60 RTXs. Then the Au-NNP(RTX) nanoassembly is obtained by adjusting the pH and the nanoassembly is formed due to the delicate balance of hydrophilic (PEG chains) and hydrophobic (RTX, LA-NR_1 and LA-NR_2) forces [30].

To detect if the obtained Au-NNP(RTX) nanoassembly could keep assembled at the physiological environment and disassemble at the tumor site, we studied the pH-responsive assembly/disassembly behavior of Au-NNP(RTX). As well known, the pH value is approximately 7.4 at the physiological environment, while the pH decreases to 6.8–6.5 at the tumor site [31]. Thus, we evaluated the morphology and size change of Au-NNP(RTX) nanoassembly. As shown in Fig. 1b and Table S1, the hydrodynamic diameters of Au-NNP(RTX) nanoassembly at pH 7.4–7.0 maintain at approximately 160 nm. When the pH ≤ 6.8, the hydrodynamic diameters decrease to 12.8 nm (6-nm Au NPs under TEM), indicating the Au-NNP(RTX) could disassemble at tumor acid environment. And as shown in Fig. 1c and d, the TEM images show that the Au-NNP(RTX) nanoassembly (<200 nm) is aggregated by 6-nm Au NPs at pH 7.4, while disassembled into uniformly dispersed 6-nm spherical structure at pH 6.8. And the zeta potential of Au-NNP(RTX) nanoassembly in Table S1 transformed from −1.5 mV to 11.8 mV, which is related to tertiary amine protonation in Fig. 1a. The nanoassembly could maintain stable and electrically neutral due to the delicate balance between the hydrophilic (PEG) and hydrophobic (RTX, LA-NR_1 and LA-NR_2) segments on the surface of Au NPs. When pH decreases, tertiary amine protonations of LA-NR_1 and LA-NR_2 make the system transform from hydrophobic to hydrophilic, the balance is broken and the nanoassembly splits into smaller Au NPs with positively electrified surface. Besides, the stability of the Au-NNP(RTX) was also studied to pledge the stability of Au-NNP(RTX) nanoassembly in subsequent applications. As shown in Fig. 1e, whether in PBS or culture medium (RPMI 1640), the sizes of Au-NNP(RTX) maintain over 150 nm, which illustrates the good stability of Au-NNP(RTX) nanoassembly.

3.2. Cellular uptake

Before cell experiment, we conducted hemolysis assay. As shown in Fig. S7, the hemolysis of RBCs with Au-NNP(RTX) nanoassembly even at the concentration as high as 200 μg/mL is lower than the recognized safe value of 5%, indicating their excellent biocompatibility.

It's reported that RTX can not only produce chemotherapy effect [32], but also has the capability to target the tumor cells with over-express folate receptor (colon cancer cell, human oral epidermoid carcinoma cell, HeLa cell, H22 cell, HCT116 cell and etc.) as a FA analog [33,34]. The previous work has proved that cellular uptake is enhanced since the ligand (FA, biotin, coumarin and glycyrrhetinic acid) shielded in the nanoassembly is exposed by pH-responsive disassembly [29]. Thus, we studied the cellular uptake of our Au-NNP(RTX) nanoassembly. First, we compared the cellular uptake of Au-NNP(RTX) nanoassembly in FA-positive cells (CT26 cells) and FA-negative cells (HepG2 cells). Au-NNP(RTX) nanoassembly is labeled with FITC (Fig. S8). For comparison, Au-NP(RTX) nanoassembly which could not disassemble at pH 7.4 and 6.8 is prepared (TEM image and UV–Vis spectrum in Fig. S9, size in Table S1) and also labeled with FITC. As shown in Fig. S10, FA-pretreated CT26 cells show less uptake than CT26 cells, which illustrates the occupied site could not bind RTX when FA binds to folate receptor in advance, and demonstrates folate receptor is indeed the binding site of RTX. Au-NNP(RTX) nanoassembly in CT26

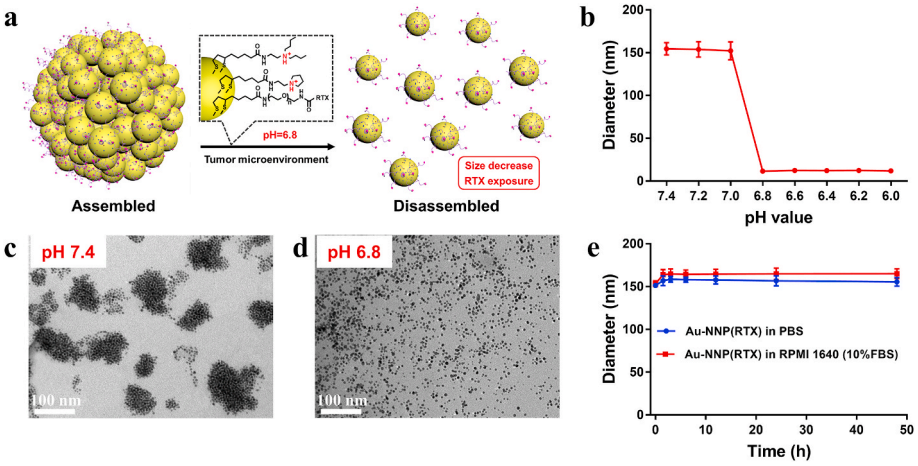

Fig. 1. pH-responsive assembly-disassembly of Au-NNP(RTX) nanoassembly. **a** disassembly process. **b** hydrodynamic diameter of Au-NNP(RTX) nanoassembly at different pHs. **c** TEM of Au-NNP(RTX) nanoassembly at pH 7.4. **d** TEM of Au-NNP(RTX) nanoassembly at pH 6.8. **e** hydrodynamic diameter of Au-NNP(RTX) nanoassembly in PBS and RPMI 1640.

cells has shown more superior cellular uptake over HepG2 cells. The mean fluorescence in CT26 cells is 2.2 times greater than in HepG2 cells. This explains RTX's better targeting capability to FA-overexpress tumor cells.

Moreover, we explored whether targeting ability of Au-NNP(RTX) nanoassembly on CT26 cells enhances through pH-responsive disassembly. We stained the cellular nucleus by DAPI and lysosome by LysoTracker Red. As shown in Fig. S11, the green fluorescence of Au-NNP (RTX) nanoassembly is evident inside the cells in both pH values and the intensity of green fluorescence in pH 6.8 group is more remarkable. It confirms that pH-responsive Au-NNP(RTX) nanoassembly has better cellular uptake at lower pH. In particular, the green fluorescence merges with red-colored lysosome. The overlay yellow fluorescence indicates that Au-NNP(RTX) nanoassembly could be taken up by CT26 tumor cells via endocytosis way. Additionally, there is almost no overlap between green fluorescent signal from FITC and blue signal from DAPI, demonstrating that Au-NNP(RTX) nanoassembly mainly stayed outside the cellular nucleus. This is mainly related to the intracellular mechanism of RTX: after it is actively transported into cells, RTX undergoes rapid, extensive metabolism by folylpolyglutamate synthetase to a series of polyglutamates (RAL-$(glu)_{3\text{-}5}$) in the cytoplasm [32]. Furthermore, As shown in Fig. 2a, very weak green signal is found in the FA-pretreated CT26 cells whether in the Au-NNP(RTX) and Au-NP(RTX) group, which is consistent with the above result. Without FA pretreatment,

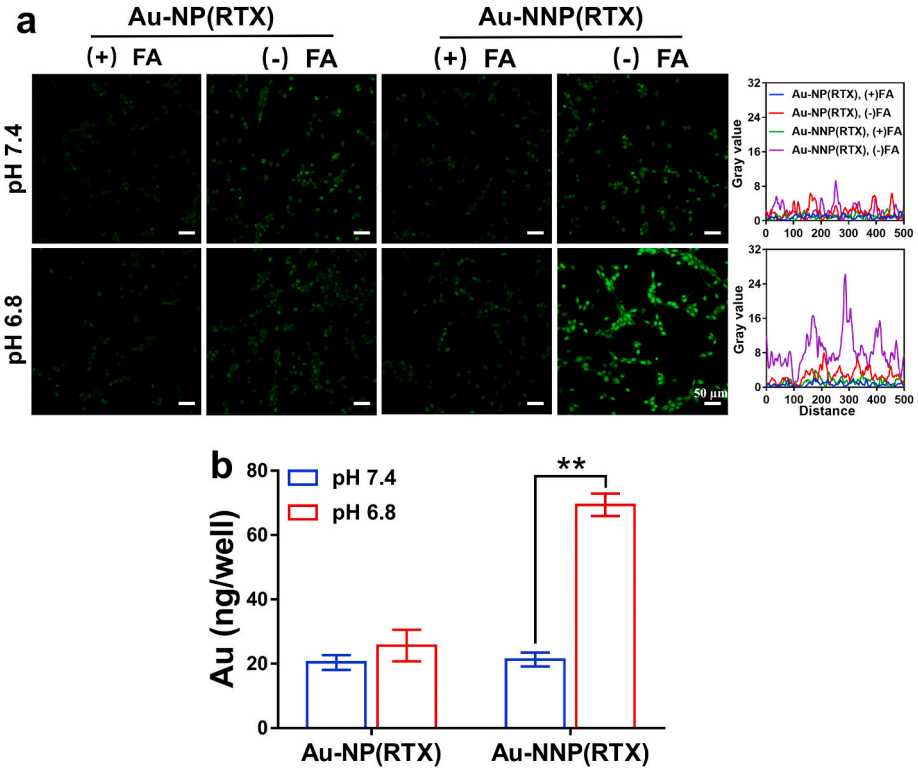

Fig. 2. Cellular uptake evaluation. **a** the CLSM images and corresponding gray value of CT26 cells dealed with FITC-labeled Au-NP(RTX) and Au-NNP(RTX) at pH 7.4 and 6.8 with or without FA pretreatment. **b** the Au element amount in CT26 cells dealed with Au-NP(RTX) and Au-NNP(RTX) at pH 7.4 and 6.8. *p < 0.05, **p < 0.01. Scale bar is 50 μm.

clear green fluorescence signals are found in both the Au-NP (RTX) groups (pH 7.4 and 6.8) and the Au-NNP(RTX) (pH 7.4), and the fluorescence intensities of these groups are similar. While at pH 6.8, the green fluorescence signal of cells in the Au-NNP(RTX) group is significantly higher than the other three groups. These results confirm that Au-NNP(RTX) nanoassembly with the disassembled capability at pH 6.8 has better uptake than the one without disassembled capability. To further verify the superiority of Au-NNP(RTX), the ICP experiment was conducted to quantitatively detect the amount of cellular uptake. As shown in Fig. 2b, the Au element amount in the cells in the Au-NNP (RTX) group at pH 6.8 is 2.25-fold higher than the one at pH 7.4. This is mainly due to the fact that Au-NNP(RTX) in the assembly state can shield RTX inside the assembly at pH 7.4, while Au-NNP(RTX) nanoassembly is disassembled at pH 6.8 and RTX is exposed. The control group at two pHs shows similar cellular uptake, both of which are similar to that of Au-NNP(RTX) at pH 7.4. This also confirms that pH-responsive disassembly could increase cellular uptake of Au-NNP (RTX) nanoassembly.

Moreover, cellular uptake of the Au-NNP(RTX) nanoassembly is also affected by radiotherapy sensitization of Au element. As shown in Fig. S12, under the irradiation of 2 Gy X-ray, it exhibits similar patterns to the CLSM images in Fig. 2a, the intensity of green fluorescence signal is all higher than those in 2a. Then, we investigated the effect of X-ray dose on the cellular uptake of Au-NNP(RTX) by ICP-AES. Here, we all simulated the micro-acid environment of the tumor (pH 6.8). As shown in Fig. S13, the cellular uptake amount increases along with the radiation dose (2–6 Gy), while not continues to increase with 8 Gy. This trend is consistent with the results of Liu's research [35]. After X-ray irradiation with a dose of 2–8 Gy, the uptake of the Au-NNP(RTX) group increases by 0.50, 0.98, 1.23, and 0.85 times, respectively, indicating the radiotherapy sensitization of Au element could enhance the cellular uptake of Au-NNP(RTX). The Au-NP(RTX) groups have similar trend and all are significantly lower than Au-NNP(RTX) groups.

The reason that X-ray sensitization increases the uptake of Au-NNP (RTX) nanoassembly was studied by cell cycle experiment. As well known, the cells mainly are in three stages (G0/G1, S and G2/M), and cellular uptake capacity is different in different phases of the cell cycle (G2/M > S > G0/G1) [35]. The cell numbers in different phases are divided by flow cytometry. The results in Fig. 3 show that without X-ray irradiation, the difference of the cell numbers in the G2/M phase between PBS, Au-NP (RTX) and Au-NNP(RTX) is not significant. After irradiation, cell numbers in the G2/M phase in the PBS group increase from 3.9% to 5.71%, indicating that ionizing radiation itself can increase cellular uptake. And cell numbers in the G2/M phase in the Au-NP(RTX) and Au-NNP(RTX) groups increase from 8.75% to 23.10%, 9.25%–34.32%, respectively. It demonstrates that X-ray irradiation could enhance cellular uptake by increasing the cell numbers in the G2/M phase.

3.3. *In vitro* therapy

After validating enhanced cellular uptake ability, the *in vitro* therapeutic effect was further evaluated. First, the cytotoxicity experiment was conducted by MTT method. As shown in Fig. 4a, the cell viability in the Au-NNP(RTX) group is lower than that of Au-NP(RTX) at the same concentration regardless of X-ray irradiation, the cytotoxicity originates from RTX which produces cytotoxic activity by the specific inhibition of thymidylate synthase [32]. It indicates that exposure of RTX by the pH-responsive disassembly enhances tumor cell targeting and chemotherapy effect. In addition, regardless of the concentration, the cytotoxicity of Au-NP(RTX) or Au-NNP(RTX) under 2-Gy X-ray irradiation is significantly higher than that of the non-X-ray group. This is ascribed to the increased uptake under X-ray irradiation and enhanced radiotherapy by Au radio-sensitization. Taking 200 μg/mL as an example, the cell killing rate in the Au-NNP(RTX) group is 54% and 1.4 times that of Au-NP(RTX) without X-ray irradiation (both of which are lower than

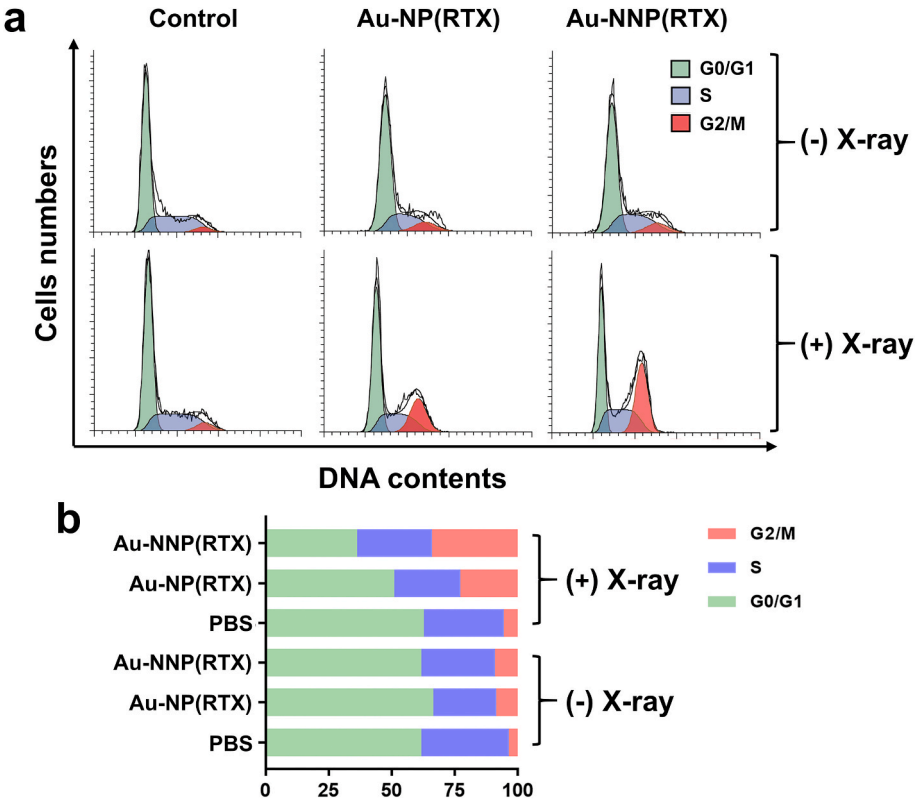

Fig. 3. The effect of X-ray on cell cycle. **a** cell cycle of PBS, Au-NP(RTX) and Au-NNP(RTX) treated CT26 cells with or without X-ray irradiation. **b** corresponding cell percentage in different phases.

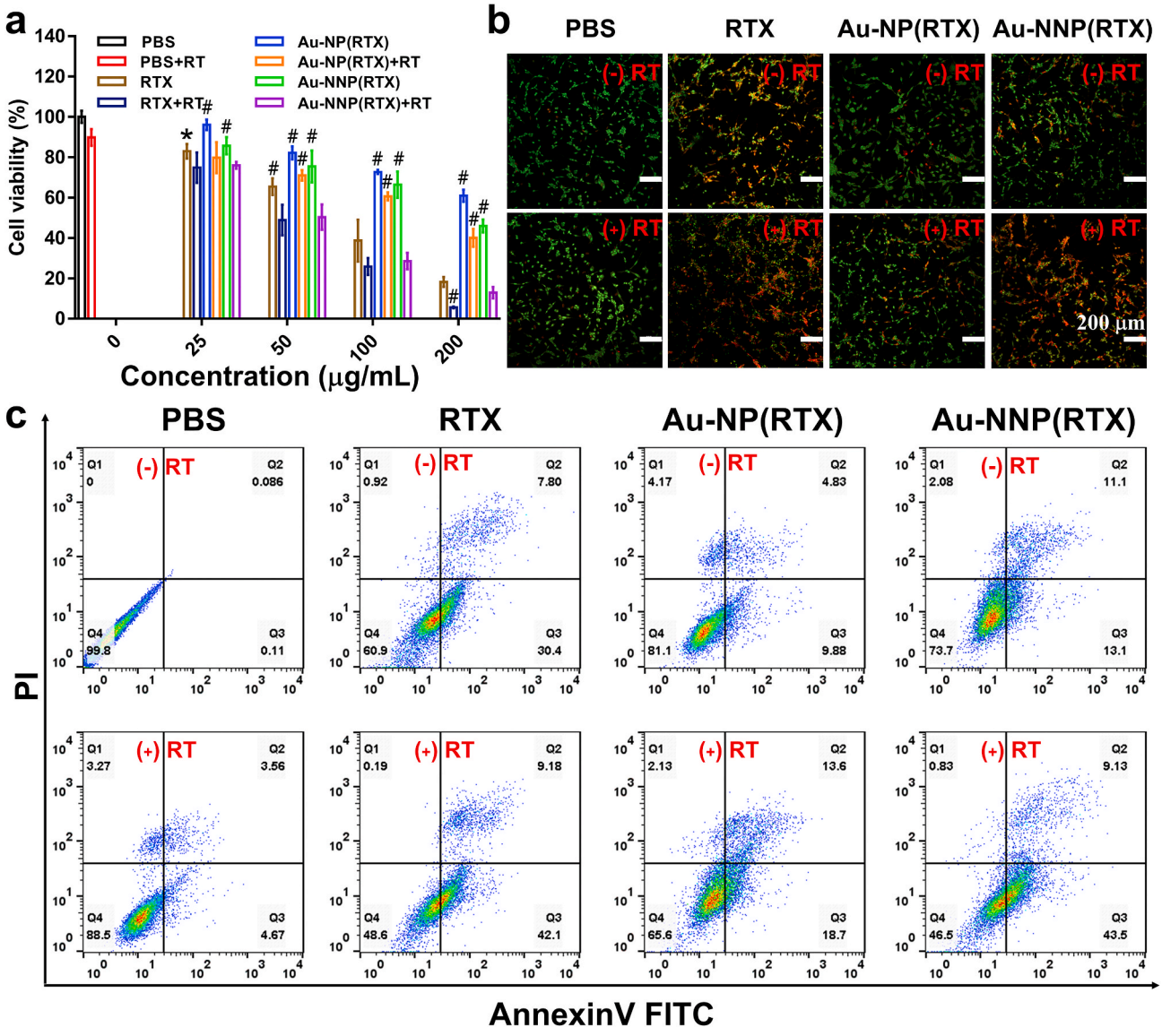

Fig. 4. *In vitro* therapy. **a** cell viability, **b** live/dead staining images and **c** apoptosis images of PBS, RTX, Au-NP(RTX), and Au-NNP(RTX) treated CT26 cells with or without X-ray irradiation. *p < 0.05, #p < 0.01 compared to Au-NNP(RTX)+RT group. Scale bar is 200 μm.

free RTX), indicating that the pH-responsive disassembly effectively increases the therapeutic effect of chemotherapy. While with 2-Gy irradiation, the cell killing rate in the Au-NNP(RTX) group is as high as 87.1%, 1.6 times that without irradiation, demonstrating that radiotherapy can further enhance the therapeutic effect of Au-NNP (RTX) except chemotherapy. The excellent synergistic results of chemo-radiotherapy provide the possibility for *in vivo* application of Au-NNP(RTX) nanoassembly.

Subsequently, live/dead staining was employed to visually observe the apoptosis of CT26 cells. AO could stain live or dead cells green, while EB could only stain dead cells red or orange. As shown in Fig. 4b, the obvious orange-red fluorescence signals are found in the RTX and Au-NNP(RTX) groups whether with or without X-ray irradiation. Moreover, under irradiation, Au-NNP(RTX) group has a brighter orange-red fluorescence signals than that without irradiation, indicating significant synergistic effect of Au-NNP(RTX) on CT26 cells. Meanwhile, the apoptosis analysis was further conducted by flow cytometry. The results in Fig. 4c and Fig. S14 show that the total apoptosis ratio of CT26 cells exposed to Au-NP(RTX) and Au-NNP(RTX) without X-ray irradiation are 14.7% and 24.2%, respectively. It demonstrates pH-responsive disassembly could enhance the killing of tumor cells. And there is a 52.6% apoptosis ratio when the CT26 cells in Au-NNP(RTX) group are exposed to X-rays, which is 28.4% higher than the one without irradiation. The enhanced apoptosis of the combined chemo-radiotherapy is consistent with MTT and live/dead staining results.

3.4. *In vitro* penetration

Given the size decrease via pH-responsive disassembly, the Au-NNP (RTX) may have better permeability in the micro-acid environment. Therefore, MCSs were employed here to explore the penetration of Cy5-labeled Au-NNP(RTX). As shown in Fig. 5, the results show that fluorescent signal in the Au-NP (RTX) group is at the edge of MCSs, whether it is at pH 7.4 or 6.8. And the fluorescent signal in the Au-NNP(RTX) group is also at the edge of MCSs at pH 7.4, while the red signals are found inside the MCSs at pH 6.8. It demonstrates that for Au-NNP(RTX), it is difficult to penetrate deep into the MCSs at physiological environment, while easy to penetrate inside the MCSs when disassembled into the Au NPs with smaller size at lower pH. At the 20–100 μm depth, the law is similar.

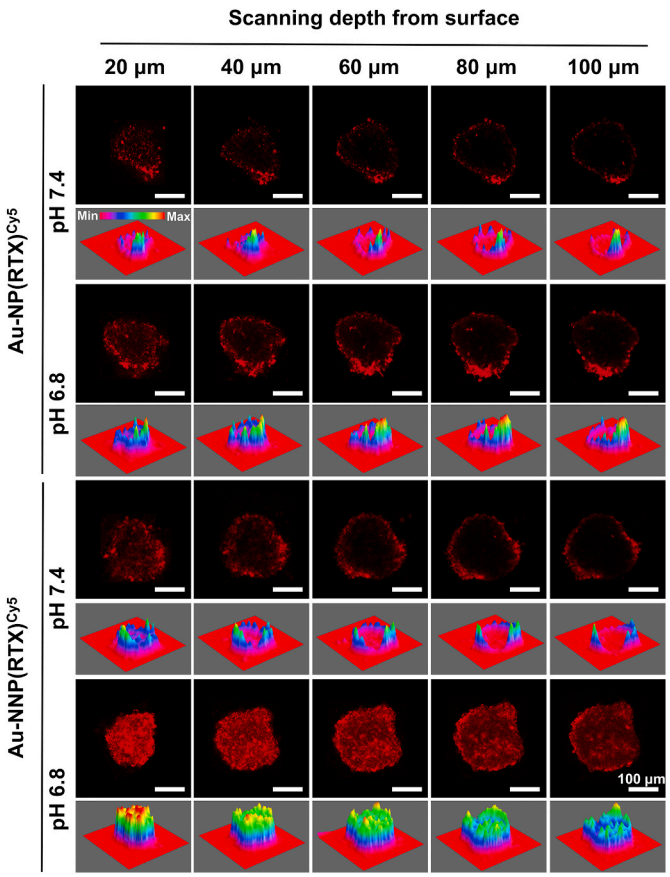

Fig. 5. *In vitro* penetration of Au-NP(RTX) and Au-NNP(RTX) into MCSs at pH 7.4 and 6.8. Scale bar is 100 μm.

3.5. In vivo penetration and accumulation

Prior to perform the *in vivo* antitumor study, we first explored the accumulation and penetration in the tumor. We have proved that Au-NNP(RTX) nanoassembly could increase cellular uptake efficiency and improve the penetration in the MCSs by pH-responsive disassembly, which may enhance the accumulation and penetration in the tumor. Here, we hired the Au-NP(RTX) used in the *in vitro* study and Au-P(RTX) (always disassembled whether at pH 7.4 and 6.8) as contrasts. The *in vivo* fluorescence imaging was employed to visually observe accumulation of Cy5-labeled Au-NNP(RTX) nanoassembly and the two contrasts. As shown in Fig. 6a and b, at 6, 12 and 24 h after injecting Cy5-labeled Au-P(RTX), Au-NP(RTX) and Au-NNP(RTX), fluorescence intensity shows significant differences and Au-NNP(RTX) group is 1.4, 1.3 and 1.8-fold that of Au-NP(RTX), 1.9, 1.7 and 2.1-fold that of Au-P(RTX) at 6, 12 and 24 h, respectively. It illustrates the fluorescence intensity in Au-NNP(RTX) group is higher than the two contrasts. The *ex vivo* fluorescence photos of heart, liver, spleen, lung, kidney and tumor excised from the mice at 24 h in Fig. S15 have shown same trend for tumors as *in vivo* fluorescence photos in 6a and 6b, and the fluorescence intensity is relatively high for liver and spleen.

Then we detected the content of Au element in the blood and tumor at 12 h. The results in Fig. 6c and Fig. S16 show that Au elements in the main organs, blood and tumor at 12 h. In Fig. S16, there are 3.41% of the injected dose (%ID) in the Au-NNP(RTX) group, 3.39 %ID in the Au-NP (RTX) group, and 1.42 %ID in the Au-P(RTX) group in the blood. Moreover, in Fig. 6c, 1.62% ID of the Au-NNP(RTX) nanoassembly has been found in the tumor, which is 1.77-fold that of Au-NP(RTX) and 2.44-fold that of Au-P(RTX). These results show that Au-NNP(RTX) has good stability in the blood and better accumulation in the tumor. And the contents of Au element in the Au-P(RTX), Au-NP(RTX) and Au-NNP (RTX) groups at different organs are obviously different. Au elements in the liver and spleen are 27.4 %ID and 17.3 %ID in the Au-NNP(RTX) group, 29.0 %ID and 16.3 %ID in the Au-NP(RTX) group, 12.3 %ID and 8.2 %ID in the Au-P(RTX) group. This indicates that NPs mainly accumulate in liver and spleen in the Au-NP(RTX) and Au-NNP(RTX) groups, while Au-P(RTX) is not only distributed in liver and spleen, but also in the kidney (7.3 %ID).

Besides, the penetration in the tumor was evaluated by CLSM. Anti-CD31/FITC and DAPI were used to label blood vessel and nuclear, respectively. As shown in Fig. 6d, for Au-NP(RTX), fluorescence signals are mainly around the blood vessels and little is found away from blood vessels. For Au-P(RTX), part of fluorescence signals is found around and

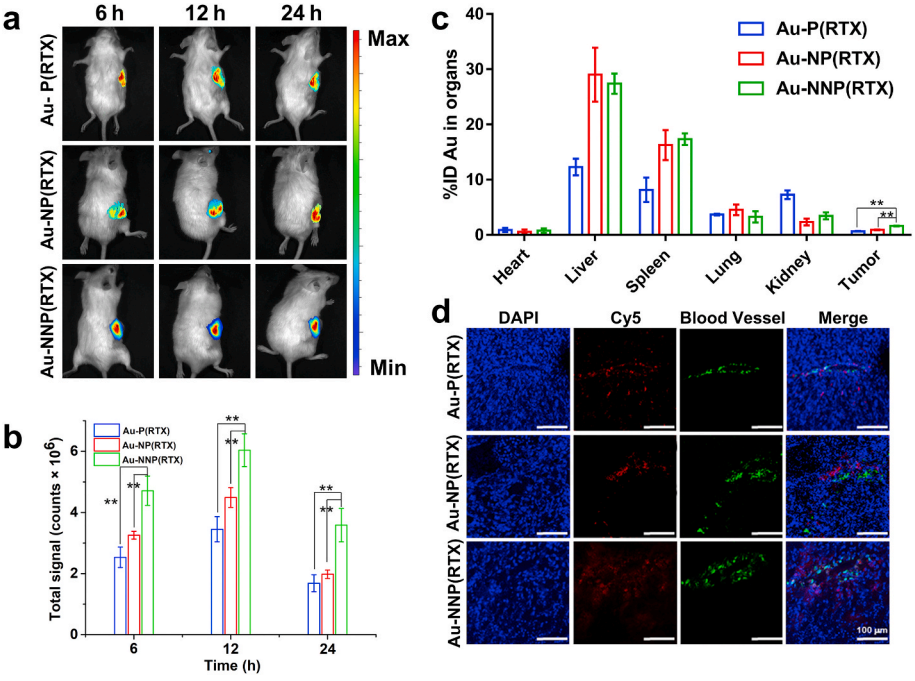

Fig. 6. *In vivo* accumulation and penetration. **a** fluorescence imaging of CT26 tumor-bearing mice and **b** quantitive fluorescence intensity of Cy5-labeled Au-P(RTX), Au-NP(RTX) and Au-NNP(RTX). **c** %ID of Au-P(RTX), Au-NP(RTX) and Au-NNP(RTX) in heart, liver, spleen, lung, kidney and tumor. **d** CLSM images of Cy5-labeled Au-P(RTX), Au-NP(RTX) and Au-NNP (RTX) after penetrating into the tumor tissue for 12 h (blue: nucleus stained by DAPI; red: Cy5 of NPs; green: anti-CD31FITC). *p < 0.05, **p < 0.01. Scale bar is 100 μm.

away from blood vessels. While the red fluorescent signals of Au-NNP (RTX) are observed both around and far away from blood vessels. Meanwhile, by analyzing fluorescence intensity at the distance (0–100 μm) from the blood vessel (Fig. S17), we find that fluorescence intensity for Au-NP(RTX) mainly concentrates within 40 μm from the blood vessel. While fluorescence intensities for the Au-P(RTX) and Au-NNP (RTX) distribute around 0–100 μm from the blood vessel, and the intensity for Au-NNP(RTX) is apparently higher than Au-P(RTX). The results demonstrate that pH-responsive Au-NNP(RTX) nanoassembly has good permeability in the tumor tissue.

3.6. *In vivo* antitumor efficacy

Encouraged by the *in vivo* accumulation and permeability, the antitumor effect of Au-NNP(RTX) was evaluated. First, the result of tumor volume change in Fig. 7a shows that the tumor volume on the mice in PBS group is the highest, followed with PBS+RT, RTX and Au-NNP (RTX). When exposure to X-ray, the tumor volume in the Au-NNP (RTX) group decreases significantly and is much lower than RTX group, which demonstrates that Au-NNP(RTX) nanoassembly accumulated at the tumor site by pH-responsive disassembly has better antitumor effect than free RTX. In addition, Au-P(RTX) and Au-NP(RTX) were also employed to conduct chemo-radiotherapy. The result shows that under the X-ray irradiation, the tumor volumes in the Au-P(RTX) and Au-NP(RTX) groups decrease to a certain extent compared to PBS group, but still significantly larger than that in the Au-NNP(RTX) group. The *ex-vivo* tumor photographs after 14-day treatment in Fig. 7b is consistent with the tumor volume result in Fig. 7a. And the result in Fig. 7c shows that the tumor inhibition rate in Au-NNP(RTX) group exposure to X-ray reaches 95.4%, which is 24.0% higher than the same group without irradiation, demonstrating the radio-sensitization effect of Au element endows the Au-NNP(RTX) excellent radiotherapy on the basis of chemotherapy. Compared with RTX+RT, Au-P(RTX)+RT and Au-NP(RTX)+RT groups, the tumor inhibition rate of Au-NNP(RTX)+RT is still highest. The H&E staining pictures of the tumor sections in Fig. 7e show the result is consistent with the above results, indicating the

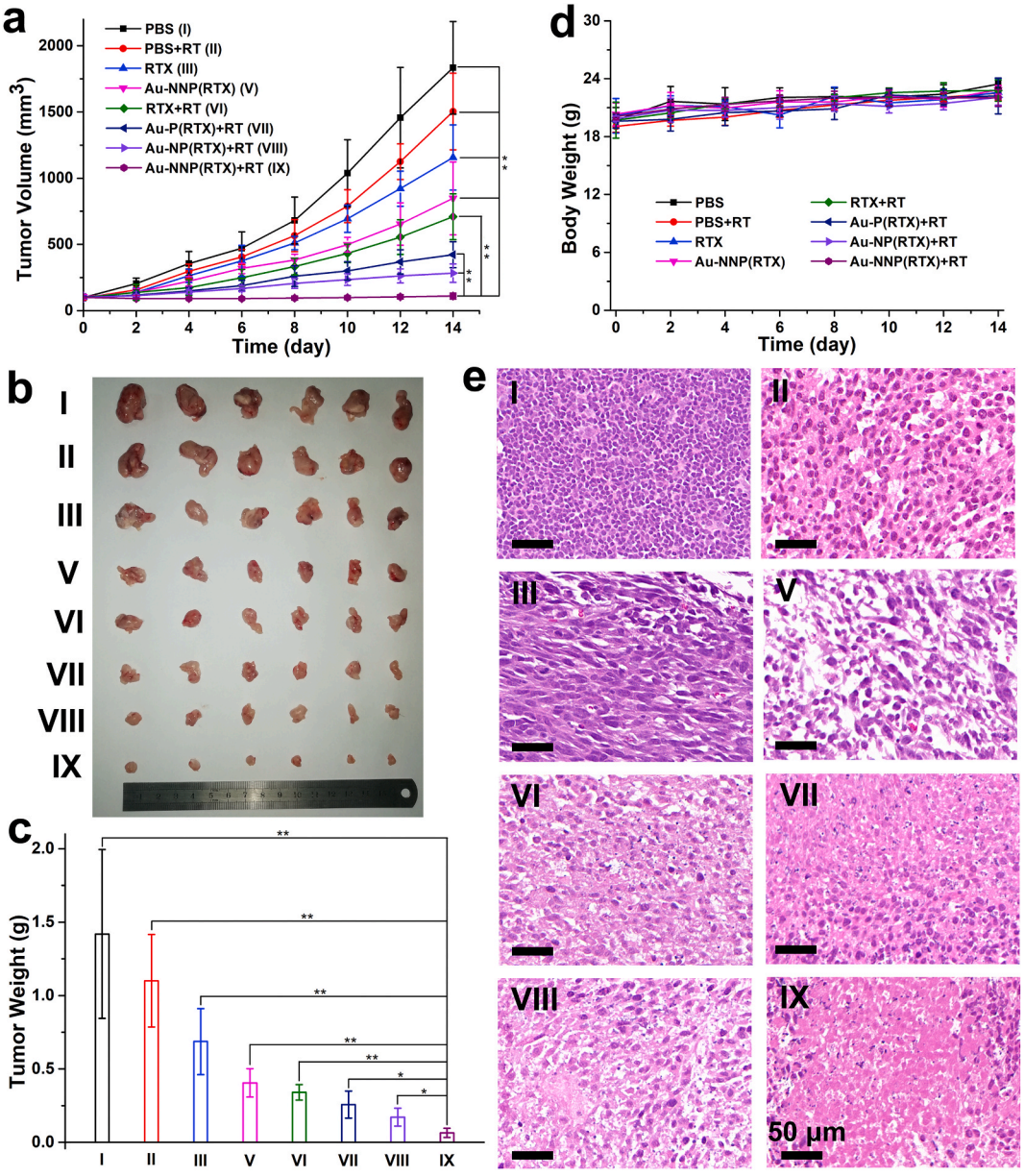

Fig. 7. *In vivo* chemo-radiotherapy. **a** tumor volume changes in 14 days. **b** photographs of the excised tumors and **c** tumor weight after 14-day treatment. **d** body weight changes in 14 days. **e** representative images of H&E staining from tumor sections after 14-day treatment. *p < 0.05, **p < 0.01. Scale bar is 50 μm.

excellent treatment effect of Au-NNP(RTX) (IX).

Moreover, as shown in Fig. 7d, during the treatment period, the body weights of BALB/c in the Au-NNP(RTX) group show no abnormal change compared to the one in the PBS group. And there is a small amount of weight loss in the RTX group, since RTX is chemical drugs, which is toxic to the body. Besides, blood biochemistry analysis of mice after intravenous injection of Au-NNP(RTX) was also studied. As shown in Fig. S18, all indicators of Au-NNP(RTX) with or without X-ray irradiation are at normal levels, and there are no statistically significant differences in biochemical indicators between the treated groups and healthy control group. These results indicate the good blood compatibility of Au-NNP(RTX). In addition, the H&E staining pictures in Fig. S19 show that the Au-NNP(RTX) did not cause any significant impact on the main organs of the mice. These results demonstrate the biosafety of Au-NNP(RTX) nanoassembly.

4. Conclusions

In summary, we have constructed an effective tumor chemo- and radio-therapeutic nanoplatform based on the pH-responsive Au-NNP (RTX) nanoassembly. The Au-NNP(RTX) nanoassembly could disassemble and split into smaller ones with large amount of RTXs on the surface at the tumor acid environment. This strategy could substantially facilitate profound tissue penetration efficacy and greatly improve tumor targeting ability of nanomedicines. Furthermore, the Au-NNP (RTX) nanoassembly exhibits excellent chemo-radiotherapy efficiency. Together, our findings suggest that this smart and versatile pH-responsive nanoassembly could be a promising approach over conventional therapeutic strategies in cancer therapy.

CRediT authorship contribution statement

Xiaomin Li: Conceptualization, Methodology, Investigation, Writing – original draft. **Licheng Yu:** Investigation, Visualization. **Chuangnian Zhang:** Resources, Investigation, Writing – review & editing, Funding acquisition. **Xiaoyan Niu:** Investigation. **Mengjie Sun:** Visualization. **Zichao Yan:** Investigation. **Wei Wang:** Writing – review & editing. **Zhi Yuan:** Conceptualization, Supervision, Writing – review & editing, Funding acquisition.

Declaration of competing interest

The authors declare that they have no known competing financial interests or personal relationships that could have appeared to influence the work reported in this paper.

Acknowledgments

This study is dedicated to 100th anniversary of Chemistry at Nankai University. This work was supported by the National Natural Science Foundation of China (Grant 52073147, 51773096, 51433004, 32071342); Specific Program for High-Tech Leader & Team of Tianjin Government, Tianjin innovation and Promotion Plan Key Innovation Team of Immunoreactive Biomaterials. We appreciate Prof. Qiang Wu at Nankai University for help with the characterization of materials and Dr. Ding Yuxun for help with characterization of penetration.

Appendix A. Supplementary data

Supplementary data to this article can be found online at https://doi.org/10.1016/j.bioactmat.2021.05.050.

References

[1] Y.S. Youn, Y.H. Bae, Perspectives on the past, present, and future of cancer nanomedicine, Adv. Drug Deliv. Rev. 130 (2018) 3–11, https://doi.org/10.1016/j.addr.2018.05.008.
[2] Q. Zhou, S. Shao, J. Wang, C. Xu, J. Xiang, Y. Piao, Z. Zhou, Q. Yu, J. Tang, X. Liu, Z. Gan, R. Mo, Z. Gu, Y. Shen, Enzyme-activatable polymer–drug conjugate augments tumour penetration and treatment efficacy, Nat. Nanotechnol. 14 (2019) 799–809, https://doi.org/10.1038/s41565-019-0485-z.
[3] C.-G. Liu, Y.-H. Han, R.K. Kankala, S.-B. Wang, A.-Z. Chen, Subcellular performance of nanoparticles in cancer therapy, Int. J. Nanomed. 15 (2020) 675–704, https://doi.org/10.2147/IJN.S226186.
[4] Q. Sun, X. Sun, X. Ma, Z. Zhou, E. Jin, B. Zhang, Y. Shen, E.A. Van Kirk, W. J. Murdoch, J.R. Lott, T.P. Lodge, M. Radosz, Y. Zhao, Integration of nanoassembly functions for an effective delivery cascade for cancer drugs, Adv. Mater. 26 (2014) 7615–7621, https://doi.org/10.1002/adma.201401554.
[5] J. Wang, W. Mao, L.L. Lock, J. Tang, M. Sui, W. Sun, H. Cui, D. Xu, Y. Shen, The role of micelle size in tumor accumulation, penetration, and treatment, ACS Nano 9 (2015) 7195–7206, https://doi.org/10.1021/acsnano.5b02017.
[6] J. Ji, F. Ma, H. Zhang, F. Liu, J. He, W. Li, T. Xie, D. Zhong, T. Zhang, M. Tian, H. Zhang, H.A. Santos, M. Zhou, Light-activatable Assembled nanoparticles to improve tumor penetration and eradicate metastasis in triple negative breast cancer, Adv. Funct. Mater. 28 (2018) 1801738, https://doi.org/10.1002/adfm.201801738.
[7] X. Zhu, C. Li, Y. Lu, Y. Liu, D. Wan, D. Zhu, J. Pan, G. Ma, Tumor microenvironment-activated therapeutic peptide-conjugated prodrug nanoparticles for enhanced tumor penetration and local T cell activation in the tumor microenvironment, Acta Biomater. 119 (2021) 337–348, https://doi.org/10.1016/j.actbio.2020.11.008.
[8] Y. Wang, S. Luo, Y. Wu, P. Tang, J. Liu, Z. Liu, S. Shen, H. Ren, D. Wu, Highly penetrable and on-demand oxygen release with tumor activity composite nanosystem for photothermal/photodynamic synergetic therapy, ACS Nano 14 (2020) 17046–17062, https://doi.org/10.1021/acsnano.0c06415.
[9] Z. Zhang, J.N. Rahmat, R. Mahendran, Y. Zhang, Controllable assembly of upconversion nanoparticles enhanced tumor cell penetration and killing efficiency, Adv. Sci. 7 (2020) 2001831, https://doi.org/10.1002/advs.202001831.
[10] Q. Hao, Z. Wang, W. Zhao, L. Wen, W. Wang, S. Lu, D. Xing, M. Zhan, X. Hu, Dual-responsive polyprodrug nanoparticles with cascade-enhanced magnetic resonance signals for deep-penetration drug release in tumor therapy, ACS Appl. Mater. Interfaces 12 (2020) 49489–49501, https://doi.org/10.1021/acsami.0c16110.
[11] X. Zhang, X. Chen, J. Song, J. Zhang, X. Ren, Y. Zhao, Size-transformable nanostructures: from design to biomedical applications, Adv. Mater. 32 (2020) 2003752, https://doi.org/10.1002/adma.202003752.
[12] J. Yan, Q. Wu, Z. Zhao, J. Wu, H. Ye, Q. Liang, Z. Zhou, M. Hou, X. Li, Y. Liu, L. Yin, Light-assisted hierarchical intratumoral penetration and programmed antitumor therapy based on tumor microenvironment (TME)-amendatory and self-adaptive polymeric nanoclusters, Biomaterials 255 (2020) 120166, https://doi.org/10.1016/j.biomaterials.2020.120166.
[13] R.K. Kankala, C.-G. Liu, D.-Y. Yang, S.-B. Wang, A.-Z. Chen, Ultrasmall platinum nanoparticles enable deep tumor penetration and synergistic therapeutic abilities through free radical species-assisted catalysis to combat cancer multidrug resistance, Chem. Eng. J. 383 (2020) 123138, https://doi.org/10.1016/j.cej.2019.123138.
[14] L. Ding, Z. Lyu, B. Louis, A. Tintaru, E. Laurini, D. Marson, M. Zhang, W. Shao, Y. Jiang, A. Bouhlel, L. Balasse, P. Garrigue, E. Mas, S. Giorgio, J. Iovanna, Y. Huang, S. Pricl, B. Guillet, L. Peng, Surface charge of supramolecular nanosystems for in vivo biodistribution: a MicroSPECT/CT imaging study, Small 16 (2020) 2003290, https://doi.org/10.1002/smll.202003290.
[15] K. Cherukula, S. Uthaman, I.-K. Park, "Navigate-dock-activate" anti-tumor strategy: tumor micromilieu charge-switchable, hierarchically activated nanoplatform with ultrarapid tumor-tropic accumulation for trackable photothermal/chemotherapy, Theranostics 9 (2019) 2505–2525, https://doi.org/10.7150/thno.33280.
[16] H.D. Summers, P. Rees, J.T.-W. Wang, K.T. Al-Jamal, Spatially-resolved profiling of carbon nanotube uptake across cell lines, Nanoscale 9 (2017) 6800–6807, https://doi.org/10.1039/C7NR01561E.
[17] Z. Hu, J. Ma, F. Fu, C. Cui, X. Li, X. Wang, W. Wang, Y. Wan, Z. Yuan, An intelligent re-shieldable targeting system for enhanced tumor accumulation, J. Contr. Release 268 (2017) 1–9, https://doi.org/10.1016/j.jconrel.2017.10.009.
[18] L. Sun, H. Wei, X. Zhang, C. Meng, G. Kang, W. Ma, L. Ma, B. Wang, C. Yu, Synthesis of polymeric micelles with dual-functional sheddable PEG stealth for enhanced tumor-targeted drug delivery, Polym. Chem. 11 (2020) 4469–4476, https://doi.org/10.1039/D0PY00653J.
[19] J. Cao, X. Gao, M. Cheng, X. Niu, X. Li, Y. Zhang, Y. Liu, W. Wang, Z. Yuan, Reversible shielding between dual ligands for enhanced tumor accumulation of ZnPc-loaded micelles, Nano Lett. 19 (2019) 1665–1674, https://doi.org/10.1021/acs.nanolett.8b04645.
[20] Y. Wen, H. Bai, J. Zhu, X. Song, G. Tang, J. Li, A supramolecular platform for controlling and optimizing molecular architectures of siRNA targeted delivery vehicles, Sci. Adv. 6 (2020), eabc2148, https://doi.org/10.1126/sciadv.abc2148.
[21] Y. Zhu, J. Zhang, F. Meng, C. Deng, R. Cheng, J. Feijen, Z. Zhong, cRGD/TAT dual-ligand reversibly cross-linked micelles loaded with docetaxel penetrate deeply into tumor tissue and show high antitumor efficacy in vivo, ACS Appl. Mater. Interfaces 9 (2017) 35651–35663, https://doi.org/10.1021/acsami.7b12439.
[22] C. Brazzale, F. Mastrotto, P. Moody, P.D. Watson, A. Balasso, A. Malfanti, G. Mantovani, P. Caliceti, C. Alexander, A.T. Jones, S. Salmaso, Control of targeting

ligand display by pH-responsive polymers on gold nanoparticles mediates selective entry into cancer cells, Nanoscale 9 (2017) 11137–11147, https://doi.org/10.1039/C7NR02595E.
[23] Z. Zhou, Y. Liu, M. Zhang, C. Li, R. Yang, J. Li, C. Qian, M. Sun, Size switchable nanoclusters fueled by extracellular ATP for promoting deep penetration and MRI-guided tumor photothermal therapy, Adv. Funct. Mater. 29 (2019) 1904144, https://doi.org/10.1002/adfm.201904144.
[24] X. Xiong, Z. Xu, H. Huang, Y. Wang, J. Zhao, X. Guo, S. Zhou, A NIR light triggered disintegratable nanoplatform for enhanced penetration and chemotherapy in deep tumor tissues, Biomaterials 245 (2020) 119840, https://doi.org/10.1016/j.biomaterials.2020.119840.
[25] X. Liu, Z. Liu, K. Dong, S. Wu, Y. Sang, T. Cui, Y. Zhou, J. Ren, X. Qu, Tumor-activatable ultrasmall nanozyme generator for enhanced penetration and deep catalytic therapy, Biomaterials 258 (2020) 120263, https://doi.org/10.1016/j.biomaterials.2020.120263.
[26] Z. Guo, J. Sui, M. Ma, J. Hu, Y. Sun, L. Yang, Y. Fan, X. Zhang, pH-Responsive charge switchable PEGylated ε-poly-l-lysine polymeric nanoparticles-assisted combination therapy for improving breast cancer treatment, J. Contr. Release 326 (2020) 350–364, https://doi.org/10.1016/j.jconrel.2020.07.030.
[27] S. Hua, J. He, F. Zhang, J. Yu, W. Zhang, L. Gao, Y. Li, M. Zhou, Multistage-responsive clustered nanosystem to improve tumor accumulation and penetration for photothermal/enhanced radiation synergistic therapy, Biomaterials 268 (2021) 120590, https://doi.org/10.1016/j.biomaterials.2020.120590.
[28] Z. Tian, C. Yang, W. Wang, Z. Yuan, Shieldable tumor targeting based on pH responsive self-assembly/disassembly of gold nanoparticles, ACS Appl. Mater. Interfaces 6 (2014) 17865–17876, https://doi.org/10.1021/am5045339.
[29] J. Ma, Z. Hu, W. Wang, X. Wang, Q. Wu, Z. Yuan, pH-sensitive reversible programmed targeting strategy by the self-assembly/disassembly of gold nanoparticles, ACS Appl. Mater. Interfaces 9 (2017) 16767–16777, https://doi.org/10.1021/acsami.7b00687.
[30] J. Ma, X. Li, Z. Hu, X. Wang, Y. Zhang, W. Wang, Q. Wu, Z. Yuan, pH-Sensitive assembly/disassembly gold nanoparticles with the potential of tumor diagnosis and treatment, Sci. China Chem. 62 (2019) 105–117, https://doi.org/10.1007/s11426-018-9354-0.
[31] H. Chen, X. Fan, Y. Zhao, D. Zhi, S. Cui, E. Zhang, H. Lan, J. Du, Z. Zhang, S. Zhang, Y. Zhen, Stimuli-responsive polysaccharide enveloped liposome for targeting and penetrating delivery of survivin-shRNA into breast tumor, ACS Appl. Mater. Interfaces 12 (2020) 22074–22087, https://doi.org/10.1021/acsami.9b22440.
[32] D. Wang, C. Yu, L. Xu, L. Shi, G. Tong, J. Wu, H. Liu, D. Yan, X. Zhu, Nucleoside analogue-based supramolecular nanodrugs driven by molecular recognition for synergistic cancer therapy, J. Am. Chem. Soc. 140 (2018) 8797–8806, https://doi.org/10.1021/jacs.8b04556.
[33] N. Gonen, Y.G. Assaraf, Antifolates in cancer therapy: structure, activity and mechanisms of drug resistance, Drug Resist. Updates 15 (2012) 183–210, https://doi.org/10.1016/j.drup.2012.07.002.
[34] Y. Zhang, M. Cheng, J. Cao, Y. Zhang, Z. Yuan, Q. Wu, W. Wang, Multivalent nanoparticles for personalized theranostics based on tumor receptor distribution behavior, Nanoscale 11 (2019) 5005–5013, https://doi.org/10.1039/C8NR09347D.
[35] X. Yi, L. Chen, J. Chen, D. Maiti, Z. Chai, Z. Liu, K. Yang, Biomimetic copper sulfide for chemo-radiotherapy: enhanced uptake and reduced efflux of nanoparticles for tumor cells under ionizing radiation, Adv. Funct. Mater. 28 (2018) 1705161, https://doi.org/10.1002/adfm.201705161.